



# Structural characterization and magnetic properties of sol–gel derived $\text{Zn}_x\text{Fe}_{3-x}\text{O}_4$ nanoparticles



E. Petrova\*, D. Kotsikau, V. Pankov

Belarusian State University, Department of Physical Chemistry, Leningradskaya Street 14, Minsk 220030, Belarus

## ARTICLE INFO

### Article history:

Received 5 May 2014

Received in revised form

22 October 2014

Accepted 25 November 2014

Available online 27 November 2014

### Keywords:

Magnetic nanoparticles

Ferrites

Sol–gel method

Structural characterization

Magnetization

## ABSTRACT

Nanocrystalline  $\text{Zn}_x\text{Fe}_{3-x}\text{O}_4$  solid solutions (with  $x=0, 0.18, 0.45, 1$ ) with crystallite sizes of 5–10 nm, specific surface of about  $180 \text{ m}^2/\text{g}$  were synthesized via an inorganic variant of the sol–gel approach. The composition and structure of the formed nanoparticles were examined with the help of powder X-ray diffraction, scanning electron microscopy, transmission electron microscopy, inductively coupled plasma atomic emission spectrometry and Fourier transform infrared spectroscopy. Hysteresis loops recorded for the samples indicate their ferromagnetic behavior at 5 K and superparamagnetic behavior at 300 K. The highest maximum magnetization of 59 emu/g at room temperature corresponds to  $\text{Zn}_{0.18}\text{Fe}_{2.82}\text{O}_4$  composition, and at 5 K to  $\text{Zn}_{0.45}\text{Fe}_{2.55}\text{O}_4$  (86 emu/g). The saturation magnetization of the pure magnetite was measured to be respectively 62 and 49 emu/g.

© 2014 Elsevier B.V. All rights reserved.

## 1. Introduction

At present time, nanosized ferrite particles with a spinel-type structure are being widely used in biology, medical diagnostics and therapy. In the case of *in vivo* applications they are mostly used in therapeutic (hyperthermia and drug-targeting) and diagnostic applications (nuclear magnetic resonance imaging (MRI)), while in the case of *in vitro* applications the main use is in diagnostics (separation/selection and magnetorelaxometry). The preparation of magnetic nanoparticles for the application in biomedicine includes such techniques as precipitation and coprecipitation from solutions, microemulsion synthesis, polyol technique, high-temperature decomposition of organic precursors, spray and laser pyrolysis etc. [1].

Magnetic nanoparticles based on iron oxides, such as magnetite ( $\text{Fe}_3\text{O}_4$ ) or maghemite ( $\gamma\text{-Fe}_2\text{O}_3$ ), are most commonly employed for biomedical applications. Superparamagnetic iron oxide nanoparticles are widely used, for example, as  $T_2$  contrast agents for MRI [2–4]. For some applications a high magnetization of the particles is also required so that their migration in blood stream could be controlled with an external magnetic field and they could be immobilized close to the target pathologic tissue [5]. However, there still remains an open challenge to improve the magnetic properties of superparamagnetic iron oxide nanoparticles, which

would lead to a higher imaging sensitivity. The vast majority of research work is devoted to the synthesis of pure oxide materials, even though the preparation of mixed oxide compositions may contribute to a considerably broader range of their functional properties. One of the ways to improve the magnetic properties of the nanoparticles is doping of magnetite with zinc with the formation of zinc ferrite–magnetite solid solutions.

The magnetic properties of zinc ferrite reported so far are related to the cation distribution [6]. Zinc ferrites are generally represented as  $(\text{Zn}_y\text{Fe}_{1-y})[\text{Zn}_{x-y}\text{Fe}_{2-x+y}]\text{O}_4$ , where the parentheses and square brackets refer to the cations occupying the tetrahedral site and the octahedral site, respectively. It has been demonstrated that the addition of  $\text{ZnFe}_2\text{O}_4$  ferrite to an inverse spinel structure (like in  $\text{Fe}_3\text{O}_4$ ) can increase the net magnetic moment of the resulting mixed spinel structure [7].

There is also another advantage of Zn-substituted iron oxide nanoparticles in comparison with other ferrites – the reduced toxicity of Zn over other metals. A preliminary *in vitro* cytotoxicity test suggests that the zinc ferrite nanoparticles possess a good safety profile [8]. For example, the Food and Drug Administration has set the reference daily intake doses for Zn at 15 mg/day, respectively, which is much higher than the Mn value (2 mg/day) [9].

A variety of methods of zinc ferrite nanoparticles preparation has been proposed. Among them are mechanical milling [10], coprecipitation method [11], rapid quenching method [12], pulsed laser deposition technique [13], sol gel route [14], approach based on oil-in-water micelles [7], sputtering method [15], solvothermal processing [16]. The reported data show that the physical and

\* Corresponding author.

E-mail addresses: [petrovaeg@bsu.by](mailto:petrovaeg@bsu.by) (E. Petrova), [kotsikau@bsu.by](mailto:kotsikau@bsu.by) (D. Kotsikau), [pankov@bsu.by](mailto:pankov@bsu.by) (V. Pankov).

chemical properties of the nanomaterials are strongly dependent on the synthetic route used.

As it was shown earlier, a modification of the sol–gel method based on inorganic precursors is a promising approach to obtain advanced metal oxide materials for different applications [17–19]. The sol–gel approach provides major possibilities to modify the grain size, the nanostructure and the phase composition of metal oxide materials, and, consequently, to tailor their functional properties over a wide range. This is achieved by varying the nature and concentration of precursors, precipitants and stabilizing agents; the temperature of the reaction mixture; the order and the rate of reagents mixing; the pH level of solutions; the mode of heat treatment of the product. The variations of the sol–gel method allow nanomaterials to be prepared in the forms of a sol, a powder, a film and ceramics. These techniques are based on the precipitation of metal hydroxides and the consecutive transformation of the precipitate into the sol, gel, xerogel and crystalline oxide [19].

For most biomedical applications, it is strictly important to obtain single-phase products homogeneous in the composition and structure. A co-precipitation of metal hydroxides and subsequent transformation of the sediment into a sol state provide a high degree of homogeneity of the starting components in reactant solutions thus promoting an efficient interaction between them. As a result, multicomponent oxide materials with a highly homogeneous structure are obtained, which cannot be achieved by using the conventional ceramic approach [20]. In the presence of bivalent metals like  $\text{Fe}^{2+}$  and  $\text{Zn}^{2+}$ , the preparation of homogeneous and stable colloidal solutions becomes a more complicated task. Therefore, a well-grounded selection of optimal reaction conditions is required.

In this study, we successfully synthesized the nanoparticles of zinc-substituted magnetite with different composition via a modified inorganic sol–gel technique. The magnetic properties and crystal structure of the  $\text{Zn}_x\text{Fe}_{3-x}\text{O}_4$  solid solutions were systematically examined in view of their potential biomedical applications.

## 2. Experimental

### 2.1. Sample preparation

Nanoparticles of  $\text{Zn}_x\text{Fe}_{3-x}\text{O}_4$  (with  $x=0.18, 0.45, 1$ ) and magnetite,  $\text{Fe}_3\text{O}_4$ , were prepared at room temperature from water solutions of inorganic salts by a modified inorganic sol–gel technique.  $\text{Fe}(\text{NO}_3)_3 \cdot 9\text{H}_2\text{O}$ ,  $\text{Zn}(\text{NO}_3)_2 \cdot 6\text{H}_2\text{O}$  and  $\text{FeSO}_4 \cdot 7\text{H}_2\text{O}$  taken in stoichiometric proportion (with 5% excess of  $\text{FeSO}_4 \cdot 7\text{H}_2\text{O}$  to compensate a possible oxidation of  $\text{Fe}^{2+}$  ions to  $\text{Fe}^{3+}$ ) were dissolved in water at room temperature to form a clear solution. To remove oxygen, water was purged with nitrogen for 40 min at the flow rate of 25 ml/s. The solutions of all salts were then mixed together under vigorous stirring with the subsequent stirring for 30 min. At this stage of the synthesis, a hydrolytic interaction between salts started due to the pH difference of the solutions of

individual salts. The solution of salts was added under vigorous stirring to a concentrated solution of NaOH, which was taken in 20 wt% excess. Under the indicated precipitation conditions, an instantaneous formation of small-sized product aggregates was achieved, which allowed us to obtain a stable colloidal solution of nanosized (less than 10 nm) particles with a narrow size distribution. The suspension was stirred for one hour to ensure the processes of hydrolysis, particle growth, polycondensation of oxo- and hydro-xocomplexes and recrystallization were completed. The described reversed order of mixing the reactants together with the excess of the precipitant provides for the preservation of phase and chemical homogeneity for each nanoparticle in the growth process since the pH of the suspension is maintained constant ( $\sim 11$ ) throughout the reaction. This pH value is sufficient for the complete deprotonation of the aquacomplexes of all three metal ions –  $\text{Fe}^{3+}$ ,  $\text{Fe}^{2+}$  and  $\text{Zn}^{2+}$ , but not for the formation of a notable amount of water-soluble metal hydroxocomplexes. Furthermore, the precipitation of mixed iron–zinc oxohydroxide with a cubic structure similar to the crystal lattice of the target spinel is expected at the early stages of the hydrolysis. A consecutive process including the formation of individual hydroxides and their interaction is not typical of the given synthesis conditions [21].

To obtain a pure product of the desired chemical composition and to ensure a long-term stability of the corresponding colloidal solution, it was necessary to remove the anions of the used salts from the resulting suspension. After the precipitate was washed with water by decantation for three times, a peptization occurred spontaneously giving a sol. The sol was stable under centrifugation at 6000 rpm due to the stabilizing effect of the residual hydroxyl ions adsorbed on the oxide aggregate. However, a significant amount of nitrate and sulfate anions remained in the sol hitherto. To remove these anions, the pH of the sol was adjusted to  $\sim 7$  by adding a 1% solution of  $\text{HNO}_3$ . At this acidity level, an isoelectric point of the oxide surface was reached causing the coagulation of the sol. The precipitate was washed with small portions of water (50 ml) three times under centrifugation, and then peptized by adding a diluted NaOH solution to the pH of 8 followed by ultrasonic treatment (3 min, 22 kHz). As a result, a stable transparent brown sol was obtained. To prepare powdered samples, the sol was dried at 60 °C in air.

### 2.2. Characterization

The phase composition and the grain size of the samples were studied by powder X-ray diffraction (XRD). The XRD analysis was carried out using  $\text{Co-K}\alpha$  radiation in the  $2\theta$  range of 10–120°. The lattice constants were refined using the RTP 3.3 X-ray structure tabular processor. The average crystallite size ( $d_{\text{XRD}}$ ) was estimated from the broadening of diffraction lines using the Scherrer's equation,  $d_{\text{XRD}} = \lambda / [(B-b)\cos\theta]$ , with the wave length  $\lambda$ , the peak width  $B$ , the instrumental broadening  $b$ , the Bragg angle  $\theta$  and the shape factor  $K \approx 0.89$ .

In addition to the XRD analysis, fine structural features of the ferrites were revealed using the infrared spectroscopy method

**Table 1**  
The results of chemical analysis (measured with ICP-AES) of the zinc-iron oxide powders prepared by the co-precipitation technique: concentrations of main constituents and of calcium oxide and silica impurities.

	Main constituents, mol%				Impurities, wt%			
	Theoretical		Experimental		Theoretical		Experimental	
	ZnO	$\text{Fe}_2\text{O}_3$	ZnO	$\text{Fe}_2\text{O}_3$	CaO	$\text{SiO}_2$	CaO	$\text{SiO}_2$
$\text{ZnFe}_2\text{O}_4$	50.0	50.0	49.8	50.2	–	–	< 0.006	< 0.006
$\text{Zn}_{0.18}\text{Fe}_{2.82}\text{O}_4$	11.3	88.7	11.6	88.4	–	–	< 0.006	< 0.006

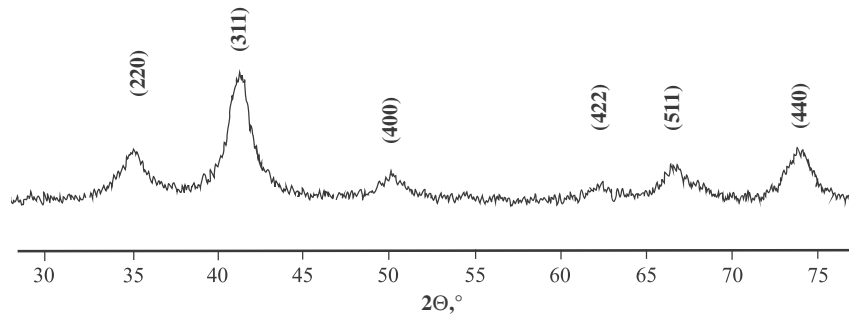


Fig. 1. The XRD pattern of the  $\text{Zn}_{0.18}\text{Fe}_{2.82}\text{O}_4$  nanoparticles.

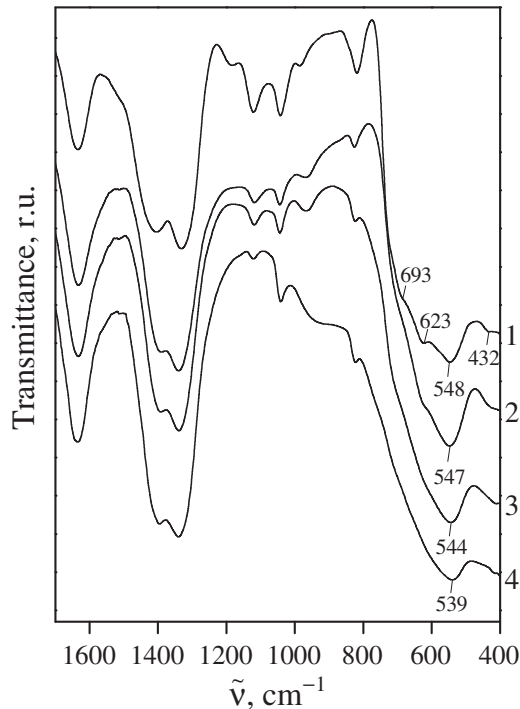


Fig. 2. Fragments of the IR spectra of the magnetite and the zinc-substituted magnetite: 1 –  $\text{Fe}_3\text{O}_4$ ; 2 –  $\text{Zn}_{0.18}\text{Fe}_{2.82}\text{O}_4$ ; 3 –  $\text{Zn}_{0.45}\text{Fe}_{2.55}\text{O}_4$ ; and 4 –  $\text{ZnFe}_2\text{O}_4$ .

(IR). IR spectra were recorded on an AVATAR FTIR-330 spectrometer supplied with a Smart Diffuse Reflectance accessory in the wavenumber ( $\tilde{\nu}$ ) range of 400–4000  $\text{cm}^{-1}$ .

The specific surface area ( $A_s$ ) of the powders was determined by nitrogen adsorption by Brunauer–Emmett–Teller (BET) method on an ASAP 2020 instrument. Assuming the spherical shape of the particles, their average size ( $d_{\text{BET}}$ ) was estimated using the relation  $d_{\text{BET}} = 6/\rho A_s$  with the density  $\rho$ .

The morphology of the materials was examined with a LEO 1420 scanning electron microscope (SEM) and a LEO 906E transmission electron microscope (TEM).

The composition of the particles was estimated by inductively coupled plasma atomic emission spectrometry (ICP-AES) with an ACTIVA-MICP-AES spectrometer.

Magnetization measurements were performed with a Cryogen Free Measurement System (CFMS) Cryogenic Ltd. Hysteresis loops,  $M(H)$ , were recorded at 5 and 300 K. The magnetization at a field of 50 kOe was taken as a maximum magnetization,  $M_{\text{max}}$ . The magnetization was also recorded as a function of temperature,  $M(T)$ , between 5 and 330 K in zero-field-cooled (ZFC) and field-cooled (FC,  $H=60$  Oe) modes, respectively.

### 3. Results and discussion

The composition of the prepared zinc-iron oxides measured by ICP-AES matches closely the theoretically calculated values. For  $\text{ZnFe}_2\text{O}_4$ , the content of zinc was found to be 49.8 mol% and for  $\text{Zn}_{0.18}\text{Fe}_{2.82}\text{O}_4$ –11.6 mol%, while the theoretical values are 50.0 and 11.3 mol%, respectively (Table 1). The concentrations of silica and calcium oxide were measured to be very low.

A typical XRD pattern of the synthesized zinc-iron oxides is shown in Fig. 1. For all samples, the only reflections attributed to a cubic spinel structure ( $Fd\bar{3}m$  space group, PDF no. 227) were observed. The observed diffraction lines are diffuse and broad, as expected due to the nanocrystalline character of the particles. The lattice constants  $a$  for the  $\text{Fe}_3\text{O}_4$ ,  $\text{Zn}_{0.18}\text{Fe}_{2.82}\text{O}_4$ ,  $\text{Zn}_{0.45}\text{Fe}_{2.55}\text{O}_4$  and  $\text{ZnFe}_2\text{O}_4$  solid solutions with average particle sizes of 5–6 nm were calculated to be 8.369, 8.391, 8.397 and 8.425 Å, respectively. It is seen that the lattice constant value increases with the increase in zinc content. The lattice constant calculated for the prepared  $\text{ZnFe}_2\text{O}_4$  is slightly smaller as compared to the stoichiometric bulk zinc ferrite ( $a=8.44$  Å), indicating that the spinel structure is cation defective and/or that the crystallization of a homogeneous spinel ferrite is not complete yet. The same decrease in the lattice constant was also observed for  $\text{Fe}_3\text{O}_4$  ( $a=8.38$  Å for bulk magnetite). Another possible explanation could be a partial oxidation of a magnetite to a maghemite,  $\gamma\text{-Fe}_2\text{O}_3$ , for which the lattice parameter is smaller (8.34 Å).

All the ferrite samples exhibit a developed specific surface area of 170–180  $\text{m}^2/\text{g}$ , which corresponds to a particle size of about 6 nm. The diameter estimated from the BET data matches closely the average particle sizes calculated by the Scherrer's equation.

To clarify the character of zinc distribution in the synthesized ferrites, IR spectroscopy was used. This method also provides additional information on the surface state of oxide materials. IR spectra of the magnetite samples heated at 50 °C with a different degree of substitution of  $\text{Fe}^{3+}$  ions with  $\text{Zn}^{2+}$  ions are compared in Fig. 2. Only the absorption bands in the wavenumber region of 400–1200  $\text{cm}^{-1}$  are shown. These bands are attributed to the stretching vibrations of  $\text{Me-O}$  ( $\nu_{\text{Me-O}}$  at 400/700  $\text{cm}^{-1}$ ) and bending vibrations of  $\text{Me-O-H}$  ( $\delta_{\text{Me-O-H}}$  at 800/1200  $\text{cm}^{-1}$ ) [22]. The occurrence of OH-groups in the ferrites is explained by the poor crystallinity of the structure and incomplete dehydration of hydroxides. In addition to the structurally bound hydroxyl groups, the presence of significant amount of adsorbed water is also typical of the xerogels of metal oxides obtained by the inorganic sol-gel method [18,19]. The adsorbed water remains in the sol-gel derived samples after their annealing at temperatures up to 600 °C. The adsorbed water was registered in the IR spectra as broad absorption bands of  $\nu_{\text{H-O-H}}$  at  $\sim 3410$   $\text{cm}^{-1}$  (not shown in the figure) and relatively narrow peaks of  $\delta_{\text{H-O-H}}$  at  $\sim 1630$   $\text{cm}^{-1}$ .

In the IR spectra of all the samples, intense absorption bands of  $\text{NO}_3^-$ -groups adsorbed on the oxide surface (1330 and 1400  $\text{cm}^{-1}$ )

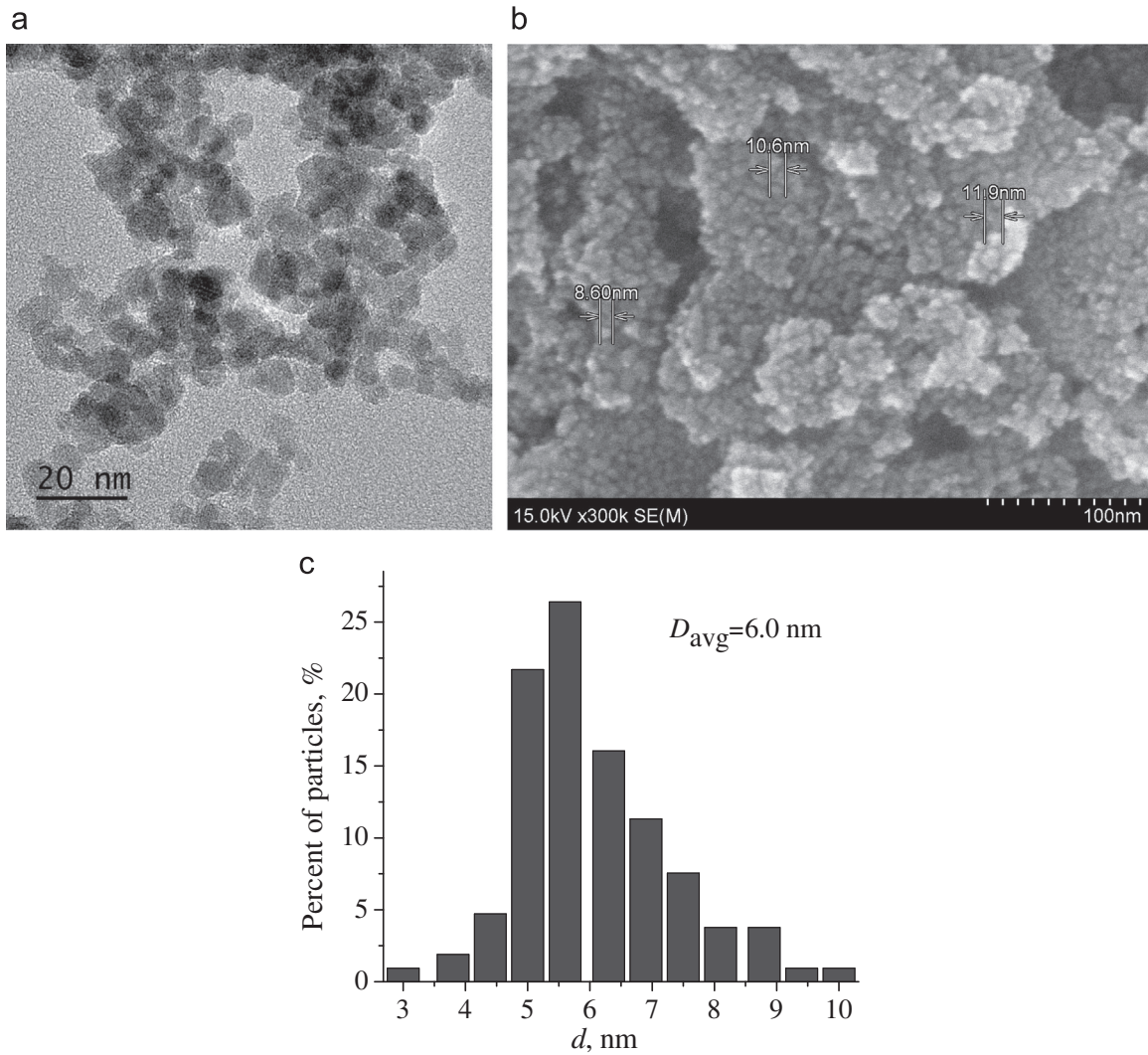


Fig. 3. The TEM (a) and SEM (b) micrographs, and the size distribution (c) of the  $Zn_{0.45}Fe_{2.55}O_4$  nanoparticles.

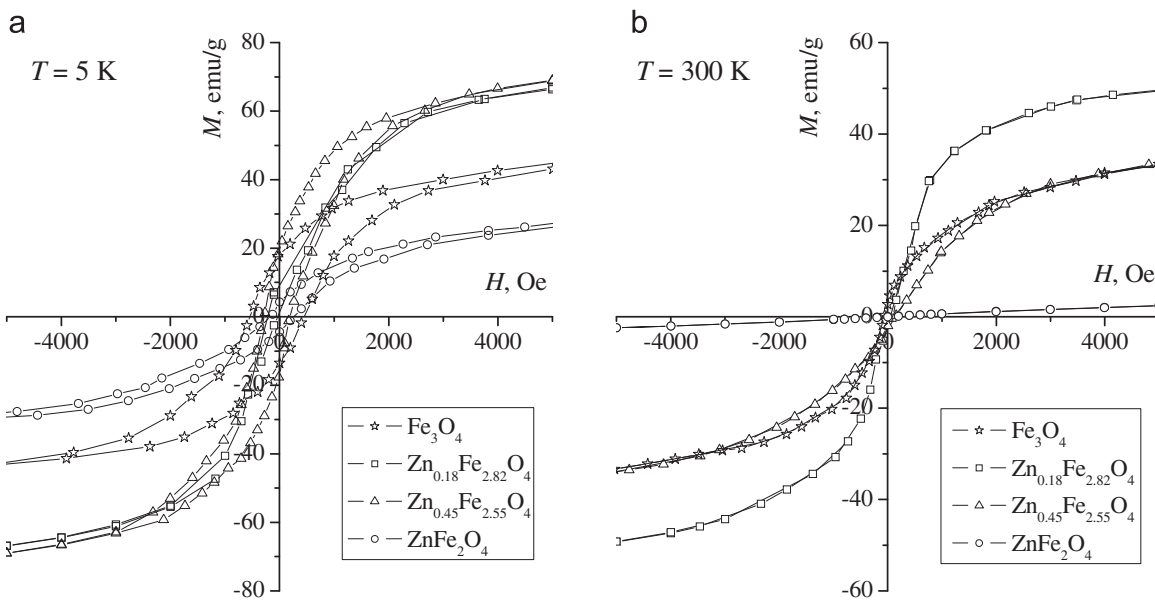


Fig. 4. The Hysteresis loops recorded for the  $Zn_{0.18}Fe_{2.82}O_4$ ,  $Zn_{0.45}Fe_{2.55}O_4$ ,  $ZnFe_2O_4$  and  $Fe_3O_4$  powders at 5 K (a) and 300 K (b).

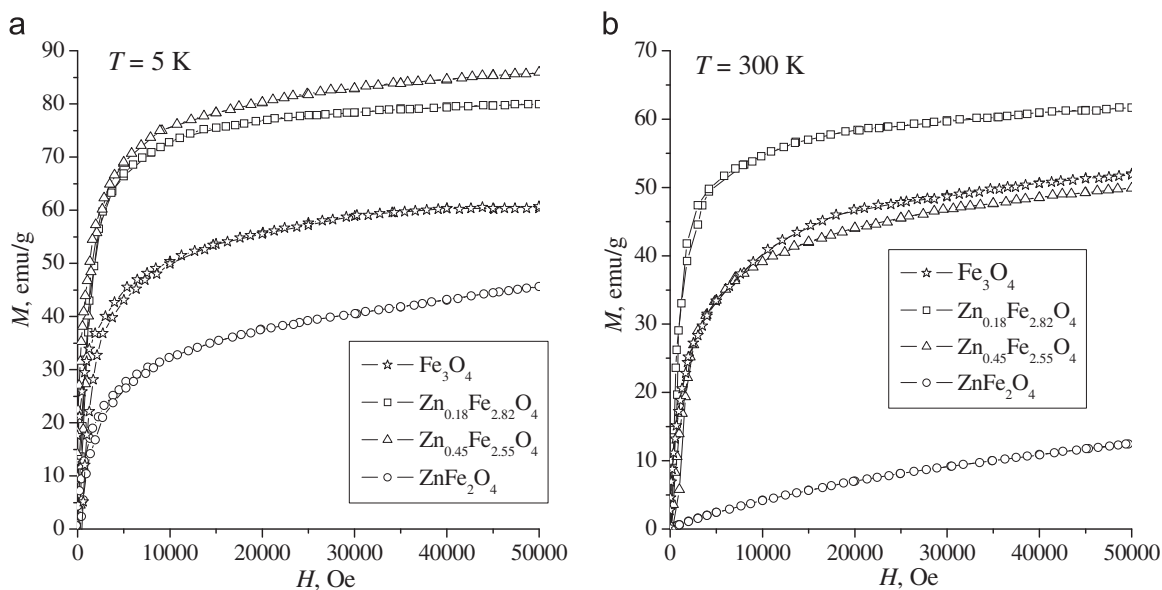


Fig. 5. The magnetization vs. field curves recorded for the  $\text{Zn}_{0.18}\text{Fe}_{2.82}\text{O}_4$ ,  $\text{Zn}_{0.45}\text{Fe}_{2.55}\text{O}_4$ ,  $\text{ZnFe}_2\text{O}_4$  and  $\text{Fe}_3\text{O}_4$  powders at 5 K (a) and 300 K (b).

Table 2

The maximum magnetization values for the  $\text{Zn}_x\text{Fe}_{3-x}\text{O}_4$  samples and the pure magnetite measured at different temperatures, blocking temperature  $T_B$  and ZFC/FC separation temperature  $T_S$  (K).

Parameter	$\text{Zn}_{0.18}\text{Fe}_{2.82}\text{O}_4$	$\text{Zn}_{0.45}\text{Fe}_{2.55}\text{O}_4$	$\text{ZnFe}_2\text{O}_4$	$\text{Fe}_3\text{O}_4$
$M_{\text{max}}$ (5 K), emu/g	80	86	45	62
$M_{\text{max}}$ (300 K), emu/g	59	46	9	49
$T_B$ (K)	100	90	25	–
$T_S$ (K)	270	220	36	–

were also observed. The presence of nitrate anion is a result of the stabilization of the colloidal solutions with nitric acid.

As may be inferred from Fig. 2, all the IR spectra differ slightly from each other. The distinctions appear as shifts of the absorption bands to lower wavenumbers as well as changes in the intensity when going from the individual magnetite to the stoichiometric zinc ferrite. This is due to the substitution of  $\text{Zn}^{2+}$  ions for  $\text{Fe}^{3+}$  ones. No absorption bands of individual zinc oxide or hydroxide were detected in the IR spectra of the samples. The reported data confirms the formation of substitutional solid solutions in the samples for all zinc concentrations studied.

The IR spectra of the samples were analyzed in more details in the region of  $400/700\text{ cm}^{-1}$ , which is characteristic of the crystalline lattice of oxides. The spectrum of the individual magnetite is in close correspondence with the reference pattern for  $\text{Fe}_3\text{O}_4$ . The characteristic absorption band for the magnetite lays at  $548\text{ cm}^{-1}$ , which is assigned to the Fe–O stretching mode induced by the interaction of the iron ions with oxygen ions in the octahedral sites of the lattice [22]. The occurrence of low-intensity additional peaks in the considered frequency range ( $432$ ,  $623$  and  $693\text{ cm}^{-1}$ ) indicates the formation of an ordered structure of cation vacancies in the octahedral sites of the inverse spinel lattice [23].

As stated earlier, in the  $\text{Zn}_x\text{Fe}_{3-x}\text{O}_4$  and the  $\text{Co}_x\text{Fe}_{3-x}\text{O}_4$  materials obtained by the combined thermal decomposition of oxalates of iron and zinc, or oxalates of iron and cobalt, the formation of substitutional solid solutions is possible in a wide range of concentrations. Iron ions occupying the tetrahedral sites of the spinel lattice are replaced with  $\text{Zn}^{2+}$  or  $\text{Co}^{2+}$  ions that should lead to the shift of the  $\nu_{\text{Fe-O}}$  vibration bands to lower frequencies due to an increased mass of  $\text{Zn}^{2+}-\text{O}^{2-}$  or  $\text{Co}^{2+}-\text{O}^{2-}$  complexes as compared

to  $\text{Fe}^{3+}-\text{O}^{2-}$  ones [24]. This was also observed for our samples with the increase in the degree of iron substitution with zinc in the magnetite. Thus, the wavenumbers of the main absorption band for  $\text{Fe}_3\text{O}_4$ ,  $\text{Zn}_{0.18}\text{Fe}_{2.82}\text{O}_4$ ,  $\text{Zn}_{0.45}\text{Fe}_{2.55}\text{O}_4$  and  $\text{ZnFe}_2\text{O}_4$  are  $548$ ,  $547$ ,  $544$  and  $539\text{ cm}^{-1}$ , respectively.

The intensity of the peaks at  $432$ ,  $623$  and  $693\text{ cm}^{-1}$  decreases with the increasing zinc content in the ferrites, which relates to a gradual disordering of the cation vacancies. There is also a similar slight shift of the band at  $548\text{ cm}^{-1}$  towards lower wavenumbers. The complete disappearance of this band confirms the formation of the normal spinel structure in the case of the  $\text{ZnFe}_2\text{O}_4$  stoichiometric ferrite.

The TEM and SEM micrographs of the ferrites given in Fig. 3 confirm the diameter of the grains ranging from 5 to 10 nm and show the grains to have a spherical shape with an average diameter of about 6 nm.

The specific magnetization of the zinc-iron oxide powders as a function of the applied magnetic field is shown Figs. 4 and 5. It can be seen that the magnetization of all the solid solutions is not completely saturated at the maximum value of the external magnetic field (50 kOe). At 5 K, all the samples show a hysteresis behavior with small coercivities (10–50 Oe depending on the sample compositions). In contrast, at 300 K, all the samples display no hysteresis. This indicates that in the prepared powders the majority of the particles have a diameter below the size critical for a superparamagnetic behavior, which is in agreement with the TEM and XRD data given above.

The maximum magnetization values measured for the Zn-doped samples at 5 and 300 K are compared with the pure nanosized magnetite in Table 2. The highest maximum magnetization of 86 emu/g measured at 5 K for the  $\text{Zn}_{0.45}\text{Fe}_{2.55}\text{O}_4$  sample exceeds noticeably the value for the  $\text{Fe}_3\text{O}_4$  powder (62 emu/g). When an external magnetic field is applied to the  $(\text{Zn}_y\text{Fe}_{1-y})[\text{Zn}_{x-y}\text{Fe}_{2-x+y}]\text{O}_4$  ferrites, the spins of atoms occupying the octahedral sites (B-sites, shown in brackets) align parallel to the direction of the external magnetic field, but those occupying the tetrahedral sites (A-sites, shown in parentheses) align antiparallel. Since the number of B-sites is twice as that of the A-sites, a non-compensated magnetic moment occurs due to the dominant A–B interactions [6,7]. This could explain the observed increase in the magnetization of the synthesized ferrites as compared to the  $\text{Fe}_3\text{O}_4$  powder prepared by using the same route.

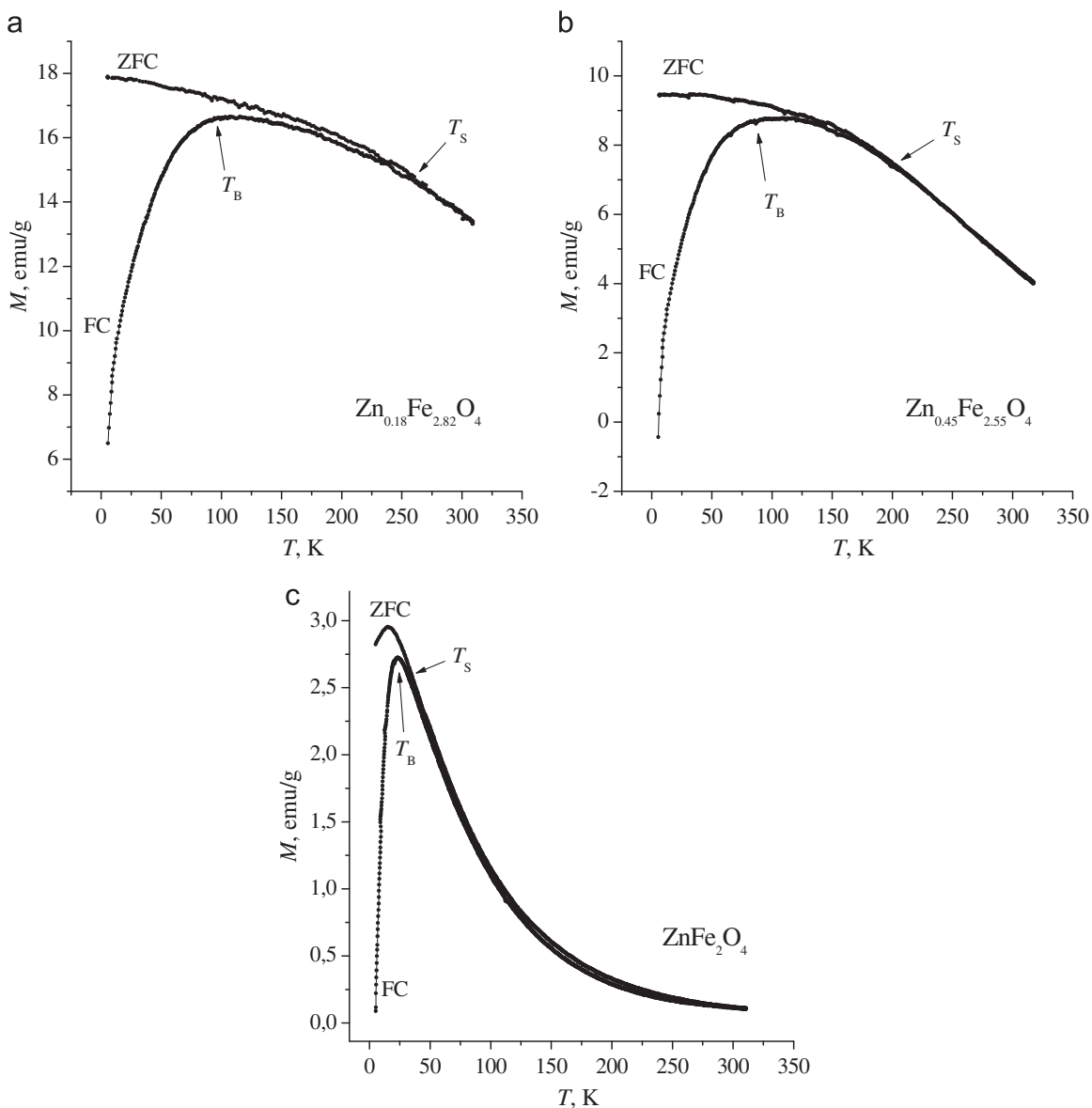


**Fig. 6.** The ZFC and FC curves recorded for the  $\text{Zn}_{0.18}\text{Fe}_{2.82}\text{O}_4$  (a),  $\text{Zn}_{0.45}\text{Fe}_{2.55}\text{O}_4$  (b) and  $\text{ZnFe}_2\text{O}_4$  (c) powders;  $H=60$  Oe.

Note that the saturation magnetization of the synthesized  $\text{Fe}_3\text{O}_4$  nanoparticles (62 emu/g) is still lower than the value for the well-crystallized bulk magnetite  $\text{Fe}_3\text{O}_4$  (96 emu/g) [25,26]. Such a reduction of the magnetization values of nanoparticles in comparison with bulk material are typical. A possible origin of this phenomenon is in the formation of a surface layer with reduced magnetization, caused by a different composition and cation distribution or disordered spins in the surface of oxides [27,28]. The bulk magnetite structure has an inversed cation distribution and antiparallel alignment of magnetic moments between the A- and B-sites of the spinel lattice.

The hysteresis measurements carried out at 300 K have shown a superparamagnetic behavior for all the synthesized nanoparticles. The highest maximum magnetization is observed for  $\text{Zn}_{0.18}\text{Fe}_{2.82}\text{O}_4$ , while for  $\text{Zn}_{0.45}\text{Fe}_{2.55}\text{O}_4$  it happened to be less than this of the magnetite. As it follows from the above results, a maximum of saturation magnetization at a certain Zn content in magnetite is expected. The maximum magnetization value measured for the stoichiometric Zn ferrite ( $\text{ZnFe}_2\text{O}_4$ ) is the lowest at both 5 and 300 K, which is evidently due to a predominant  $\text{Zn}^{2+}$  occupation of A sites instead of B sites in the spinel lattice leading to a decrease in the magnetic parameters of the material.

The ZFC and FC measurements of the  $\text{Zn}_{0.18}\text{Fe}_{2.82}\text{O}_4$  and  $\text{Zn}_{0.45}\text{Fe}_{2.55}\text{O}_4$  samples represented in Fig. 6-a and b show a behavior typical of superparamagnetic particles with a significant width of the particle size distribution. The ZFC and FC curves are separate from each other at  $T_S$  and goes through a maximum at blocking temperature  $T_B$  [29]. The analysis of the ZFC/FC curves can provide some additional information about the cluster state of the sample. The derivative of this curve is correlated with the temperature distribution of the energy barrier, which in turn is connected with a particle size distribution. The separation point position of ZFC/FC curves corresponds to the maximum blocking temperature (and a maximum particle size), whereas the peak position on an ZFC curve corresponds to the average blocking temperature value [30]. The relatively small difference between  $T_B$  and  $T_S$  ( $\sim 10$  K) and a sharp FC maximum in Fig. 6-c indicates a narrow particle size distribution for  $\text{ZnFe}_2\text{O}_4$ , which was not observed for both  $\text{Zn}_{0.18}\text{Fe}_{2.82}\text{O}_4$  and  $\text{Zn}_{0.45}\text{Fe}_{2.55}\text{O}_4$  compositions. This unusual FC curve maximum has already been reported for other oxide nanomaterials [31,32]. On one hand, Testa et al. [33] have recently suggested that the presence of a maximum on ZFC curve for spinel-type iron oxides is the result of the combination of

the blocking of the magnetic moment of each particle and the magnetic interactions between the particles. On the other hand, Pileni et al. [34] have claimed that in nonstoichiometric zinc ferrite it is due to the intrinsic ferrimagnetic structures of the particles.

ZFC curves recorded for  $\text{Zn}_{0.18}\text{Fe}_{2.82}\text{O}_4$ ,  $\text{Zn}_{0.45}\text{Fe}_{2.55}\text{O}_4$  and  $\text{ZnFe}_2\text{O}_4$  all display a maximum, indicating a transition to a superparamagnetic behavior. The comparison of the blocking temperatures for zinc ferrites, however, is ambiguous because of the difference in the iron content as well as in the inversion degree of the cations distribution. For the  $\text{ZnFe}_2\text{O}_4$  sample, the blocking temperature is much lower than that measured for the other compositions, which indicates a wider temperature range of superparamagnetism for the  $\text{ZnFe}_2\text{O}_4$  nanoparticles.

#### 4. Conclusion

Zinc-iron oxide nanoparticles ( $\text{Zn}_x\text{Fe}_{3-x}\text{O}_4$ , where  $x=0, 0.18, 0.45, 1$ ) were synthesized via a modified inorganic sol–gel technique. The particles exhibit a crystallite size of 5–10 nm and a superparamagnetic behavior at room temperature.

The IR spectroscopy data have revealed the substitution of  $\text{Fe}^{3+}$  ions in the tetrahedral and octahedral positions of the  $\text{Fe}_3\text{O}_4$  spinel lattice with  $\text{Zn}^{2+}$  ions with the formation of substitutional solid solutions over a wide range of concentrations.

A hysteresis behavior is observed for all samples at 5 K. The highest maximum magnetization of 59 emu/g at 300 K corresponds to the  $\text{Zn}_{0.18}\text{Fe}_{2.82}\text{O}_4$  sample, and at 5 K – to the  $\text{Zn}_{0.45}\text{Fe}_{2.55}\text{O}_4$  sample (86 emu/g), both exceeding the maximum magnetization of the pure magnetite (62 and 49 emu/g, respectively) due to the dominant A–B cation interactions.

It has been demonstrated that the chosen approach is applicable to a room temperature synthesis of single-phase  $\text{Zn}_x\text{Fe}_{3-x}\text{O}_4$  ferrites in a nanosized state.

The synthesized ferrites can be potentially used as materials for electronics and as contrasting agents for magnetic resonance imaging.

#### References

- [1] P. Tartaj, M. Puerto Morales, S. Veintemillas-Verdaguer, T. Gonzalez-Carreño, C. J. Serna, *J. Phys. D: Appl. Phys.* 36 (2003) R182–R197.
- [2] S. Mornet, S. Vasseur, F. Grasset, E. Duguet, *J. Mater. Chem.* 14 (2004) 2161–2175.
- [3] D.L. Thorek, A.K. Chen, J. Czupryna, A. Tsourkas, *Ann. Biomed. Eng.* 34 (2006) 23–38.
- [4] J. Wan, W. Cai, X. Meng, E. Liu, *Chem. Commun.* (2007) 5004–5006.
- [5] A. Jordan, R. Scholz, K. Maier-Hauff, et al., *J. Magn. Magn. Mater.* 225 (2001) 118–126.
- [6] H.H. Hamdeh, J.C. Ho, S.A. Oliver, et al., *J. Appl. Phys.* 81 (1997) 1851–1857.
- [7] J. Hocheplied, P. Bonville, M. Pileni, *J. Phys. Chem. B* 104 (2000) 905–912.
- [8] J. Wan, X. Jiang, H. Li, K. Chen, *J. Mater. Chem.* 22 (2012) 13500–13505.
- [9] S.B. Goldhaber, *Regul. Toxicol. Pharmacol.* 38 (2003) 232–242.
- [10] C.N. Chinnasamy, A. Narayanasamy, N. Ponpandian, et al., *J. Phys.: Condens. Matter* 12 (2000) 7795–7805.
- [11] T. Kamiyama, K. Haneda, T. Sato, et al., *Solid State Commun.* 81 (1992) 563–566.
- [12] K. Tanaka, M. Makita, Y. Shimizugawa, et al., *J. Phys. Chem. Solids* 59 (1998) 1611–1618.
- [13] Y. Yamamoto, H. Tanaka, T. Kawai, *Jpn. J. Appl. Phys.* 40 (2001) L545–L547 Part 2.
- [14] A. Azam, M. Chaman, A.H. Naqvi, *Int. J. Nanopart.* 2 (2009) 388–393.
- [15] S. Nakashima, K. Fujita, K. Tanaka, K. Hirao, *J. Phys.: Condens. Matter* 17 (2005) 137–149.
- [16] S. Surinwong, A. Rujiwatra, *Particuology* 11 (2013) 588–593.
- [17] L.V. Interrante, L.A. Caspar, A.B. Ellis, *Materials Chemistry. An Emerging Discipline*, American Chemical Society, Washington (1995) 555.
- [18] M. Ivanovskaya, P. Bogdanov, A. Gurlo, *Proceedings of the VIII International Meetings of Chemical Sensors*, Basel, Switzerland, 2000, pp. 94.
- [19] C.J. Brinker, G.W. Scherer, *Sol–Gel Science: the Physics and Chemistry of Sol–Gel Processing*, Academic Press, London (1990) 502pp..
- [20] V.V. Pankov, *Mater. Sci. Eng. A224* (1997) 101–106.
- [21] D. Kotsikau, M. Ivanovskaya, A. Taurino, P. Siciliano, in: V.E. Borisenko, et al., (Eds.), *Mater. Int. Conf. Nanomeeting-2007* (Minsk, Belarus, 22–25 May), World Scientific, Singapore, 2007, pp. 372–376.
- [22] K. Nakamoto, *Infrared and Raman Spectra of Inorganic and Coordination Compounds*, Part B, 6th edition, Wiley, New York (2009) pp. 424.
- [23] B. Gillot, R.M. Benloucif, A. Rousset, *J. Solid State Chem.* 39 (4) (1981) 329–336.
- [24] B. Gillot, F. Jemmal, A. Rousset, *J. Solid State Chem.* 50 (2) (1983) 138–145.
- [25] J. Mürbe, A. Rechtenbach, J. Töpfer, *Mater. Chem. Phys.* 110 (2008) 426–433.
- [26] J.M.D. Coey, D. Khalafalla, *Phys. Status Solidi (A)* 11 (1972) 229–241.
- [27] J. Mürbe, A. Rechtenbach, J. Topfer, *Mater. Chem. Phys.* 110 (2008) 426–433.
- [28] V. Sepalak, I. Bergmann, A. Feldhoff, et al., *J. Phys. Chem. C* 111 (2007) 5026–5033.
- [29] M.H. Dodson, E. McClelland-Brown, *J. Geophys. Res.* B 85 (5) (1980) 2625–2637.
- [30] U. Voskoboinik, *Acta Phys. Pol. A* (92 Suppl.) (1997) S43.
- [31] R.D. Zysler, D. Fiorani, A.M. Testa, *J. Magn. Magn. Mater.* 224 (2001) 5–11.
- [32] G. Goya, H. Rechenberg, M. Chen, W. Yelon, *J. Appl. Phys.* 87 (2000) 8005–8007.
- [33] A.M. Testa, *J. Magn. Magn. Mater.* 224 (2001) 5–11.
- [34] P. Pileni, J. Hocheplied, M. Bonville, *J. Phys. Chem. B* 104 (2000) 905–912.